An Arp2/3 nucleated F-actin shell fragments nuclear membranes at nuclear envelope breakdown in starfish oocytes

Masashi Mori[1], Kálmán Somogyi[1], Hiroshi Kondo[1], Nilah Monnier[3,4], Henning J. Falk[1], Pedro Machado[2], Mark Bathe[3,5], François Nédélec[1], and Péter Lénárt[1*]

[1]Cell Biology and Biophysics Unit and [2]Electron Microscopy Core Facility, European Molecular Biology Laboratory (EMBL), Meyerhofstrasse 1, Heidelberg, D-69117, Germany

[3]Laboratory for Computational Biology & Biophysics, Department of Biological Engineering, Massachusetts Institute of Technology (MIT), 77 Massachusetts Avenue, Cambridge MA 02139, USA

[4]Harvard Biophysics Program, Massachusetts Hall, Cambridge MA 02138, USA

[5]Broad Institute of MIT and Harvard, 301 Binney Street, Cambridge MA 02142, USA

[*]Correspondence: lenart@embl.de

Running title: **An F-actin shell breaks the nuclear envelope**

Highlights

- An F-actin ‘shell’ assembles underneath the nuclear envelope at NEBD in oocytes
- This transient F-actin shell is nucleated by the Arp2/3 complex
- The F-actin shell functions to fragment nuclear membranes in NEBD
- Preventing F-actin shell formation in meiosis leads to formation of aneuploid eggs

Summary

Animal cells disassemble and reassemble their nuclear envelopes (NE) upon each division [1, 2]. Nuclear envelope breakdown (NEBD) serves as a major regulatory mechanism by which mixing of cytoplasmic and nuclear compartments drives the complete reorganization of cellular architecture, committing the cell for division [2, 3]. Breakdown is initiated by phosphorylation-driven partial disassembly of the nuclear pore complexes (NPCs), increasing their permeability, but leaving the overall NE structure intact [4–7]. Subsequently, the NE is rapidly broken into membrane fragments, defining the transition from prophase to prometaphase and resulting in complete mixing of cyto- and nucleoplasm [6, 8]. However, the mechanism underlying this rapid NE fragmentation remains largely unknown. Here, we show that NE fragmentation during NEBD in starfish oocytes is driven by an Arp2/3 complex nucleated F-actin 'shell' that transiently polymerizes on the inner surface of the NE. Blocking the formation of this F-actin shell prevents membrane fragmentation and delays entry of large cytoplasmic molecules into the nucleus. We observe spike-like protrusions extending from the F-actin shell that appear to 'pierce' the NE during the fragmentation process. Finally, we show that NE fragmentation is essential for successful reproduction, because blocking this process in meiosis leads to formation of aneuploid eggs.

Results and Discussion

An F-actin shell polymerizes transiently underneath the NE at NEBD

Although fragmentation of the NE has been studied in various model organisms and has been proposed to have important functions in cell division, the mechanisms that drive NE fragmentation during NEBD remain poorly understood [1, 2]. In mammalian fibroblasts, centrosomal microtubules tear open and remove the NE from the nuclear surface [8, 9], but it is unclear to what extent this process contributes to actual membrane fragmentation. Importantly, such a microtubule-driven mechanism is unlikely to be sufficient in cell types such as large oocytes with disproportionately large nuclei compared to the size of microtubule asters. Indeed, NE fragmentation is known to be independent of microtubules in starfish oocytes [6], clearly requiring the existence of alternative mechanisms. In previous studies, we noted a bright, dense and transient shell of F-actin of unknown function that polymerizes along the NE around the time of NEBD in starfish oocytes [10]. The temporal and spatial proximity of this F-actin shell to NE fragmentation suggested that it may play a role in promoting fragmentation.

Using fast 3D imaging, we find that the F-actin shell initiates at a few individual foci on the NE and then rapidly spreads to engulf the entire nucleus in ~1 min (Fig. 1A). This F-actin shell can be observed along the NE by a variety of live-cell F-actin markers [10] and by phalloidin staining in fixed cells (Fig. 1A-D). High resolution light microscopy confirms previous findings by immunogold electron microscopy (EM) [10] that the F-actin shell forms on the inner, nuclear side of the NE (Fig. 1E). The F-actin shell then depolymerizes in ~1 min (Fig. 1A), with the exception of dense patches of F-actin surrounding chromosomes close to the nuclear periphery (Fig. S1A-E). The shell forms concomitantly with the network of F-actin bundles in the nuclear region that we have shown previously to drive chromosome congression [10, 11], but is distinct in structure and molecular composition (Fig. S1F, G).

The F-actin shell is nucleated by the Arp2/3 complex

Based on the dense morphology of the F-actin shell, we hypothesized that the Arp2/3 complex might be involved in its nucleation. Indeed, we observe specific localization of mEGFP-tagged Arpc1, a subunit of the Arp2/3 complex, to the F-actin shell but not to the F-actin bundle network (Fig. 1F). This localization is confirmed by immunofluorescence labeling using an anti-Arpc1 antibody (Fig. S1H). Consistent with Arpc1 localization, we find that treatment of oocytes with the small-molecule Arp2/3 inhibitor CK-666, but not its inactive analog CK-689 [12], abolishes formation of the F-actin shell, but does not prevent formation of the bundle network (Fig. 1G-I, Fig. S1I and Movie S1). Many CK-666 treated oocytes still retain small remnants of F-actin foci along the NE at NEBD, but these foci do not spread into a full F-actin shell (Fig. 1G, H). These remnants likely result from incomplete inhibition of Arp2/3, due to the relatively low affinity of CK-666 [12]. To quantify our observations of shell inhibition, we measured mean F-actin fluorescence intensity along the nuclear rim and found that CK-666 effectively blocks the transient enrichment of F-actin in the rim region that is seen in DMSO-treated control oocytes (Fig. 1I). Together, these data indicate that the Arp2/3 complex is required specifically to nucleate the F-actin shell, but not the F-actin bundle network, during NEBD.

The F-actin shell is required for timely and complete permeabilization of the NE

Previous studies of NEBD in starfish oocytes have shown that NE fragmentation begins at a single or few foci and then rapidly spreads from these locations along the NE. This pattern of NE fragmentation can be inferred from the kinetics of entry of large cytoplasmic molecules into the nuclear region [7] and directly visualized by fast imaging of live oocytes and by electron microscopy [6]. Although polymerization of the F-actin shell along the NE occurs at roughly the same time as NE fragmentation, earlier data did not allow us to dissect the temporal order of these events [10]. Using improved markers and imaging conditions, here we find that the earliest F-actin foci form ~30 s before the entry of large cytoplasmic molecules (160 or 500 kD dextrans) into the nuclear region (Fig. 2A, Movie S2). This temporal offset rules out the possibility that the shell forms as a consequence of NE fragmentation. Subsequently, as the F-actin foci spread along the NE and merge into a continuous

shell, dextran entry begins exactly at the site where the foci first appeared and spreads in the same pattern as the F-actin shell, continuing to lag the shell by ~30 s (Fig. 2A).

To test whether there is a causal relationship between these two processes, as suggested by their tight spatiotemporal correlation, we followed the kinetics of dextran entry in oocytes treated with CK-666 to block formation of the F-actin shell (Fig. 2B, C). Previous studies have shown that initial entry of small (25 kD) dextran occurs via NPC disassembly early in NEBD, when nuclear membranes are still intact, while entry of large (160 or 500 kD) dextran requires NE fragmentation [6]. As expected, the initial entry kinetics of 25 kD dextran through NPCs prior to membrane fragmentation are not affected by CK-666 treatment (Fig. 2C, -5–0 minutes, gray lines), confirming that the F-actin shell and Arp2/3 complex are not involved in NPC disassembly, which is driven by phosphorylation of nucleoporins [5]. In contrast, entry of 160 kD dextran is considerably delayed in CK-666 treated oocytes (Fig. 2B, C, colored lines, Movie S2), implying a role for the F-actin shell in NE fragmentation. Interestingly, it is the rate of entry rather than the start time of entry that is affected, with a roughly 2-fold reduction in the peak entry rate (Fig. 2C, inset). To exclude any non-specific effects of CK-666, we confirmed this delay in dextran entry in oocytes treated with cytochalasin D or latrunculin B to prevent actin polymerization altogether (Fig. S2A). Finally, because those drugs may have side effects that damage the cell cortex, we also injected excess phalloidin into oocytes prior to NEBD to drive all cellular actin into stabilized cytoplasmic filament bundles and thereby prevent formation of any new F-actin structures without damaging the cell cortex. Phalloidin injection effectively blocks F-actin shell formation (data not shown) and delays entry of the 160 kD dextran in a manner indistinguishable from CK-666 treatment (Fig. 2B, C).

To explore how the observed change in dextran entry kinetics could be caused by altered properties of NE fragmentation in the absence of the F-actin shell, we performed quantitative simulations of dextran entry using a model previously developed by Terasaki et al. [7], in which a spherical NE contains an area of permeabilization (fragmentation) that can vary in size and permeability to diffusing dextran molecules (Fig. S2B). We defined the initiation site and growth rate of the

permeabilization area based on experimental observations, and fit the diffusion coefficient of the dextran molecules to match the entry kinetics observed in control oocytes [6]. With these parameters, the model closely reproduces the experimentally observed spatial and temporal kinetics of dextran entry in control oocytes (Fig. 2D, E). In this model, a delay in dextran entry could be caused by a reduction either in the rate at which the area of permeabilization grows over time or in its permeability to dextran. We found that the best fit to the delayed dextran entry kinetics observed in oocytes treated with CK-666 is obtained when the speed of spreading is reduced by 2.3-fold and the permeability is reduced by 25-fold (Fig. 2D, E and Fig. S2C).

Taken together, these dextran results indicate that formation of the transient F-actin shell, as mediated by Arp2/3, is required for efficient fragmentation of the NE at NEBD; in the absence of the F-actin shell, the NE remains largely intact. This reduction in permeability could be caused by a failure of initial breakpoints in the NE to expand and efficiently fragment NE membranes, consistent with our observation that only the rate of dextran entry but not the start time of entry is affected by treatment with CK-666.

Inhibition of the F-actin shell leaves the NE intact after NEBD

As NE fragmentation can be resolved by electron microscopy (EM) [6], we sought to directly visualize fragmentation in the presence and absence of the F-actin shell. To support these data with larger sample numbers, we additionally developed a light microscopy fragmentation assay based on immunostaining of NPCs in fixed oocytes. Unlike in somatic cells, the NE of oocytes is tightly packed with NPCs, which form a dense array with ~150 nm spacing (Fig. 3A). Therefore, the intact NE before NEBD appears in deconvolved light microscopy images as a homogeneous grainy surface and a thin continuous line in cross section (Fig. 3B). In contrast, the fragmented NE after NEBD appears in cross section as a broader fragmented line by light microscopy, consistent with the NE fragments visualized in cross section by EM (compare Fig. 3A and B). The surface view of the NE after NEBD in deconvolved light microscopy images reveals a network of NE fragments (Fig. 3B), as was presumed but not yet directly reconstructed from thin section EM data.

In stark contrast to control oocytes, in oocytes treated with CK-666 we observe that the NE remains intact after NEBD by both EM and NPC staining (Fig. 3C). These intact NE membranes are observed for more than 20 min after NEBD (Fig. 3C, 'late stage'). The occurrence of NEBD was confirmed in these samples by the disappearance of the smooth and sharp NE boundary in transmitted light microscopy and the folded morphology of the NE apparent by EM, and by co-staining the F-actin bundle network in the nuclear region by fluorescence microscopy (Fig. 3C). To quantify NE fragmentation, we traced NE fragments on large EM montages of the entire nuclear region after NEBD (Fig. 3D and Fig. S3) and found a 25-fold difference in average fragment length of 1.40±0.17 µm in DMSO control (n=5 oocytes) compared to 35.51±28.86 µm in CK-666 treated oocytes (n=4 oocytes). Although these parameters are measured on 2D thin sections and are not directly interpretable in terms of 3D structure, they provide clear evidence for a large difference in membrane morphology in the absence of the F-actin shell. Finally, we confirmed these results in live cells by labeling the NE with the nucleoporin POM121-EGFP3 (Fig. 3E). In live CK-666 treated or phalloidin injected oocytes, the NE boundary remains a thin and continuous line after NEBD that is clearly separated from the bulk ER, in contrast to control oocytes in which the broadening and roughening of the NE boundary after NEBD is clearly observed (Fig. 3E). Identical observations were made in oocytes treated with cytochalasin D or latrunculin B (Fig. S2). Therefore, direct observation of the NE in both live and fixed cells indicates that blocking formation of the F-actin shell prevents NE fragmentation during NEBD.

The F-actin shell fragments nuclear membranes at NEBD

Finally, we combined this live-cell NE fragmentation assay with F-actin co-labeling, in order to directly determine when and where NE fragmentation occurs relative to formation of the F-actin shell. Individual frames of live cell recordings capture the process of spreading of the F-actin shell, and these frames contain both intact and fragmented portions of the NE as visualized by both NPC and lamina (lamin B-EGFP) markers (Fig. 4A, B). We observe that the NE is consistently intact in regions where the F-actin shell is not yet present, whereas regions of the NE underlined by the F-actin shell

appear fragmented (Fig. 4A, B). These results indicate that fragmentation of the NE is rapid and is tightly correlated in space and time with F-actin shell formation. Fixed oocytes with partially formed F-actin shells confirm that fragmentation is spatially correlated with the presence of the F-actin shell (Fig. 4C). With the high spatial resolution of these fixed samples, we also observe spike-like F-actin structures, similar in morphology to filopodia that protrude from the F-actin shell and appear to project through the NE (Fig. 4C, arrowheads). These structures are even more prominent in cells fixed in a buffer optimized to preserve F-actin (Fig. 4D). To determine whether these F-actin projections might affect NE morphology, we examined the NE in detail in EM samples fixed during this shell formation stage. We observe very unusual spike-like protrusions of the NE (Fig. 4E) that are fully consistent in size and number with the F-actin protrusions visualized by light microscopy. Interestingly, these protrusions are specifically localized to portions of the NE that are still intact but adjacent to fragmented regions (Fig. 4E), suggesting that they relate to the mechanism by which fragmentation spreads along the NE.

Conclusions

In conclusion, we have revealed a novel mechanism of NE fragmentation during NEBD that is mediated by an Arp2/3 nucleated shell of F-actin. This F-actin shell spreads along the NE concurrently with visible fragmentation of the NE and its permeabilization to large molecules. The shell is not involved in initial permeabilization, because entry of large dextrans begins at the same time in both control oocytes and oocytes in which shell formation is blocked. However, the rate of entry is significantly reduced in the absence of the F-actin shell, indicating that the shell is required for the rapid spread of NE fragmentation that quickly and completely permeabilizes the NE. In analogy to a dam on a river, the downstream area can be flooded either slowly through small leaks or rapidly by a massive breach. The F-actin shell is required to convert initial leaks in the NE into a massive breach. These initial leaks are believed to form when the core NPC structure disassembles [6, 7]. We hypothesize that these leaks allow cytoplasmic Arp2/3 complexes to enter the nucleus and nucleate the initial foci of F-actin seen along the NE (Fig. 1A, arrowheads). These initial foci rapidly grow and

spread along the NE through the self-amplifying mechanism of Arp2/3 [13, 14], forming a complete F-actin shell that drives massive fragmentation of the NE by a mechanism that likely involves the spike-like protrusions that we observe to pierce the NE. Although we have shown that Arp2/3 is the major nucleator involved in shell formation, our present data do not exclude the possibility that additional nucleators and other actin regulators associate with the F-actin shell, in a manner similar to lamellipodia formation [15]. Indeed, the long and bundled appearance of the spike-like protrusions suggests the involvement of filament cross-linkers and straight filament nucleators.

In somatic cells, it is widely accepted that rapid breakdown and removal of the NE from the nuclear surface at NEBD is important to allow timely progression of cell division, because intact nuclear membranes physically hinder cytoplasmic microtubules from gaining access to chromosomes [8]. Here we find that inefficient NE fragmentation in the absence of the F-actin shell has a dramatic effect on chromosome congression, with over 70% of CK-666 treated oocytes failing to collect all chromosomes to the meiotic spindle by anaphase onset, leading to the formation of aneuploid eggs (Fig. S4 and Movie S3). Thus, rapid and complete fragmentation of the NE is essential for normal progression through meiosis in oocytes as much as for mitosis in somatic cells. It is, however, unclear at present how broadly this F-actin driven mechanism of NE fragmentation is conserved across species and cell types. Bright, dense and transient F-actin shells along the NE during NEBD have been observed in early embryos of diverse echinoderm species including sea urchin, starfish and sand dollars ([16] and our unpublished data). Thus, this mechanism is likely required for mitosis in early embryos as well as oocytes, at least in echinoderms. Notably, in most other species NEBD has not been characterized in such detail, and therefore it remains an open question whether this mechanism is conserved across other phyla.

Supplemental Data

Supplemental Data include Experimental Procedures, four figures, and three movies and can be found with this article online.

Acknowledgements

We would like to thank Jan Ellenberg and Nathalie Daigle (EMBL) for support in the early phase of the project and for comments on the manuscript. We thank Mark Terasaki (University of Connecticut Health Center) for his constant support throughout the project. We also thank Melina Schuh (MRC Laboratory of Molecular Biology) and Bill Bement (University of Wisconsin Madison) for comments on the manuscript. We would like to acknowledge the essential support of EMBL's Electron Microscopy Core Facility, specifically the help of Rachel Mellwig and Yannick Schwab. We thank Beáta Bugyi (University of Pécs) for providing purified tropomyosin and Arp2/3, Art Hand (University of Connecticut Health Center) for sharing EM protocols, Patrick Leahy (Caltech) and Trevor Fay (Monterey Abalone) for supplying starfish animals.

This research was funded by EMBL and the Deutsche Forschungsgemeinschaft (DFG) research grant SPP1464 EL 246/5-1 and LE 2926/1-1 to Jan Ellenberg and P. L., respectively. M.M. was additionally supported by the Uehara Memorial Foundation. N.M. and M.B. were supported by MIT Faculty Start-up Funds, and N.M. was additionally supported by a National Science Foundation Graduate Research Fellowship. Part of this work was performed at the Marine Biological Laboratory (Woods Hole, MA).

References

1. Burke, B., and Ellenberg, J. (2002). Remodelling the walls of the nucleus. Nat. Rev. Mol. Cell Biol. *3*, 487–497.

2. Güttinger, S., Laurell, E., and Kutay, U. (2009). Orchestrating nuclear envelope disassembly and reassembly during mitosis. Nat. Rev. Mol. Cell Biol. *10*, 178–191.

3. Hetzer, M. W. (2010). The nuclear envelope. Cold Spring Harb. Perspect. Biol. *2*, a000539.

4. Dultz, E., Zanin, E., Wurzenberger, C., Braun, M., Rabut, G., Sironi, L., and Ellenberg, J. (2008). Systematic kinetic analysis of mitotic dis- and reassembly of the nuclear pore in living cells. J. Cell Biol. *180*, 857–865.

5. Laurell, E., Beck, K., Krupina, K., Theerthagiri, G., Bodenmiller, B., Horvath, P., Aebersold, R., Antonin, W., and Kutay, U. (2011). Phosphorylation of Nup98 by multiple kinases is crucial for NPC disassembly during mitotic entry. Cell *144*, 539–550.

6. Lénárt, P., Rabut, G., Daigle, N., Hand, A. R., Terasaki, M., and Ellenberg, J. (2003). Nuclear envelope breakdown in starfish oocytes proceeds by partial NPC disassembly followed by a rapidly spreading fenestration of nuclear membranes. J. Cell Biol. *160*, 1055–1068.

7. Terasaki, M., Campagnola, P., Rolls, M. M., Stein, P. A., Ellenberg, J., Hinkle, B., and Slepchenko, B. (2001). A new model for nuclear envelope breakdown. Mol. Biol. Cell *12*, 503–510.

8. Beaudouin, J., Gerlich, D., Daigle, N., Eils, R., and Ellenberg, J. (2002). Nuclear envelope breakdown proceeds by microtubule-induced tearing of the lamina. Cell *108*, 83–96.

9. Mühlhäusser, P., and Kutay, U. (2007). An in vitro nuclear disassembly system reveals a role for the RanGTPase system and microtubule-dependent steps in nuclear envelope breakdown. J. Cell Biol. *178*, 595–610.

10. Lénárt, P., Bacher, C. P., Daigle, N., Hand, A. R., Eils, R., Terasaki, M., and Ellenberg, J. (2005). A contractile nuclear actin network drives chromosome congression in oocytes. Nature *436*, 812–818.

11. Mori, M., Monnier, N., Daigle, N., Bathe, M., Ellenberg, J., and Lénárt, P. (2011). Intracellular transport by an anchored homogeneously contracting f-actin meshwork. Curr. Biol. CB *21*, 606–611.

12. Nolen, B. J., Tomasevic, N., Russell, A., Pierce, D. W., Jia, Z., McCormick, C. D., Hartman, J., Sakowicz, R., and Pollard, T. D. (2009). Characterization of two classes of small molecule inhibitors of Arp2/3 complex. Nature *460*, 1031–1034.

13. Hetrick, B., Han, M. S., Helgeson, L. A., and Nolen, B. J. (2013). Small molecules CK-666 and CK-869 inhibit actin-related protein 2/3 complex by blocking an activating conformational change. Chem. Biol. *20*, 701–712.

14. Pollard, T. D. (2007). Regulation of Actin Filament Assembly by Arp2/3 Complex and Formins. Annu. Rev. Biophys. Biomol. Struct. *36*, 451–477.

15. Ridley, A. J. (2011). Life at the Leading Edge. Cell *145*, 1012–1022.

16. Burkel, B. M., von Dassow, G., and Bement, W. M. (2007). Versatile fluorescent probes for actin filaments based on the actin-binding domain of utrophin. Cell Motil. Cytoskeleton *64*, 822–832.

17. Riedl, J., Crevenna, A. H., Kessenbrock, K., Yu, J. H., Neukirchen, D., Bista, M., Bradke, F., Jenne, D., Holak, T. A., Werb, Z., et al. (2008). Lifeact: a versatile marker to visualize F-actin. Nat. Methods *5*, 605–607.

Figure legends

Figure 1. An Arp2/3 nucleated F-actin shell forms transiently along the NE at NEBD in starfish oocytes

(A) Maximum intensity Z-projections of the nuclear region of a live oocyte expressing mEGFP3-UtrCH (the calponin homology domain of human utrophin protein tagged with three mEGFPs [16]) to visualize the formation, spreading, and disassembly of the F-actin shell. The cell cortex has been segmented out to allow visualization of the cell interior. Times are shown relative to the start of NEBD. Red arrowheads mark initial F-actin foci.

(B) Partially-formed F-actin shell in an oocyte fixed during NEBD and stained with Alexa488-phalloidin. Maximum intensity Z-projection of the entire nuclear region (left) and a selected single confocal section (right) are shown.

(C) Single confocal section through a partially-formed F-actin shell labeled by the Lifeact-EGFP F-actin marker [17] in a live oocyte.

(D) Single confocal section through an almost fully-formed F-actin shell labeled by rhodamine-actin in a live oocyte.

(E) *Left:* Deconvolved confocal section through the NE of an oocyte fixed during NEBD and stained with mAb414 to label NPCs (cyan) and Alexa568-phalloidin to label the F-actin shell (red). *Right:* Intensity profile for the two channels along the dashed line marked on the image at left.

(F) Confocal sections through the nuclear region of a live oocyte expressing the Arp2/3 complex subunit mEGFP-Arpc1 (gray) and injected with $DiIC_{18(3)}$ to label membranes (red) and histone H1-Alexa647 to label chromosomes and also the nucleolus (cyan), revealing specific recruitment of Arpc1 to the F-actin shell.

(G) Confocal sections through the nuclear regions of live oocytes expressing mEGFP3-UtrCH (gray) and injected with $DiIC_{18(3)}$ (red), incubated for 1 h with either 0.5 mM CK-666 or a corresponding amount of DMSO prior to NEBD.

(H) Fraction of oocytes with complete or near complete inhibition of the F-actin shell for the CK-666 versus DMSO treatment conditions as in (G). Oocytes were scored for the presence or absence of the F-actin shell, and n is the number of oocytes imaged in each condition.

(I) Mean F-actin intensity along the NE measured from time-lapse recordings such as those shown in (G). The NE was automatically segmented by thresholding of the $DiIC_{18(3)}$ channel at each time point. Mean mEGFP3-UtrCH intensity measurements along the segmented NE were normalized such that control oocytes ranged from 0 to 1. Averages (solid lines) and standard deviations (shaded regions) of the normalized mean intensity are shown for 5 oocytes each for both CK-666 and DMSO treatment.

Times are given as mm:ss relative to NEBD, and scale bars are 20 μm except for (E) where the sale bar is 5 μm.

Figure 2. The F-actin shell is required for timely and complete permeabilization of the NE

(A) *Top:* Confocal sections through the nuclear region of a live oocyte expressing mEGFP3-UtrCH (cyan) and injected with Cy5 labeled 500 kD dextran (red), showing the tight spatial and temporal correlation between F-actin shell formation and dextran entry. *Bottom:* mEGFP3-UtrCH and 500 kD dextran intensity along a portion of the NE (as marked on the leftmost image above), shown 'unrolled' into a straight line. On the far right is an overlay of the mEGFP3-UtrCH and dextran channels with a 32-second time shift to highlight the precise spatial correlation between F-actin shell formation and dextran entry.

(B) Confocal sections through the nuclear region of live oocytes co-injected with Cy5 lableled 25 and TRITC labeled 160 kD dextrans, and either incubated with DMSO, CK-666 or injected with an excess

of phalloidin prior to NEBD. The 160 kD dextran channel is shown, demonstrating the delay in dextran entry upon interference with F-actin shell formation.

(C) Quantification of mean nuclear fluorescence intensity (measured within the dashed circles shown in (B)) for the 25 and 160 kD dextran channels (gray and colored lines, respectively) for oocytes treated with DMSO, CK-666 or injected with phalloidin as shown in (B). Averages (solid lines) and standard deviations (shaded regions) of mean intensity from at least 5 oocytes are shown. The mean intensity values are normalized for each condition by defining zero as the mean of the measurements between -5 and -4 minutes and one as the mean of the measurements between 9 and 11 minutes. *Inset:* Rate of change of the mean nuclear fluorescence intensity, reflecting the rate of dextran entry into the nuclear region, calculated using a moving average of 10 frames.

(D) Simulated dextran entry kinetics (dashed lines) compared to experimentally measured entry kinetics (thin solid lines with standard deviations) of the 160 kD dextran for CK-666 and DMSO treated oocytes (same data as (C) except re-normalized between 1 and 11 minutes).

(E) Comparison of the spatial pattern of 160 kD dextran entry for experiments (upper panels) versus simulation (lower panels) for the CK-666 and DMSO treated oocytes, as in (B).

Times are shown relative to the initiation of F-actin shell formation in mm:ss, and scale bars are 20 µm, except for the lower panels of (A) where the scale bar is 5 µm.

Figure 3. Preventing F-actin shell formation leaves the NE intact

(A) Thin section electron micrographs of the NE in an oocyte fixed before NEBD (top row) and an oocyte fixed approximately 3-5 min after NEBD (bottom row), visualizing NE fragmentation during NEBD. Inset shows a surface view of the NE tightly packed with NPCs. Scale bars are 1 µm, or 0.5 µm for the top right panel.

(B) Fluorescent staining of the NE by mAb414 (gray) and F-actin by phalloidin (red) in an oocyte fixed before NEBD (top row) and an oocyte fixed after NEBD (bottom row), visualizing NE fragmentation by

light microscopy. *Left column:* Single confocal sections of the nuclear region from deconvolved 3D datasets. *Middle column:* Enlarged view of the NE (corresponding to the dashed rectangles at left). *Right column:* Enlarged surface view of the NE taken from a confocal section at the bottom of the nuclear region. Scale bars are 20 µm (left column) or 5 µm (middle and right columns).

(C) Electron micrograph and immunostaining of the NE after NEBD in oocytes treated with CK-666. Samples were processed together with the control samples shown in (A) and (B). The rightmost image shows an oocyte treated with CK-666 and fixed approximately 20 min after NEBD. Scale bars are as in (A) and (B).

(D) Thin section EM montage of the entire nuclear region of oocytes fixed after NEBD and treated with CK-666 (right) or a corresponding concentration of DMSO (left). Traced NE fragments are shown in red overlay. For the raw EM images see Fig. S3. Scale bars are 5 µm.

(E) Single confocal sections through a portion of the nuclear region of live oocytes expressing the nucleoporin POM121-mEGFP3 to label the NE. Sections are shown before NEBD and after NEBD for an oocyte incubated with DMSO (top panels), and after NEBD for oocytes incubated with CK-666 or injected with an excess of phalloidin (bottom panels). Scale bars are 5 µm.

Figure 4. The F-actin shell fragments nuclear membranes at NEBD

(A) Deconvolved confocal section of the nuclear region of an oocyte expressing POM121-mEGFP3 (red) and mEGFP3-UtrCH (cyan) during formation of the F-actin shell, revealing the tight correlation between the presence of the F-actin shell and fragmentation of the adjacent NE. Enlarged regions of the NE, as marked on the leftmost image (numbers), are shown at right for each channel and as an overlay. Scale bars are 20 and 5 µm, for the overview and enlarged regions, respectively.

(B) Same as (A) for an oocyte expressing lamin B-EGFP instead of POM121-mEGFP3 to label the NE.

(C) Fluorescent staining of the NE by mAb414 (red) and F-actin by Alexa568-phalloidin (cyan) in an oocyte fixed during formation of the F-actin shell. Enlarged regions of the NE, as marked on the

leftmost image (numbers), are shown at right ‘unrolled’ into straight lines. Arrowheads highlight prominent spike-like protrusions of the F-actin shell. Scale bars are 20 and 1 µm, for the overview and enlarged regions, respectively.

(D) Phalloidin staining of an oocyte fixed during formation of the F-actin shell with a buffer optimized to preserve F-actin. A single confocal section from a deconvolved 3D dataset is shown (left), along with an enlarged view of the NE (right). Scale bars are 20 and 5 µm, for the overview and enlarged regions, respectively.

(E) Thin section electron micrograph of an oocyte fixed during fragmentation of the NE, showing spike-like protrusions of the NE at the boundary between intact (left) and fragmented (right) sections of the NE. Scale bar is 1 µm.

Figure 1

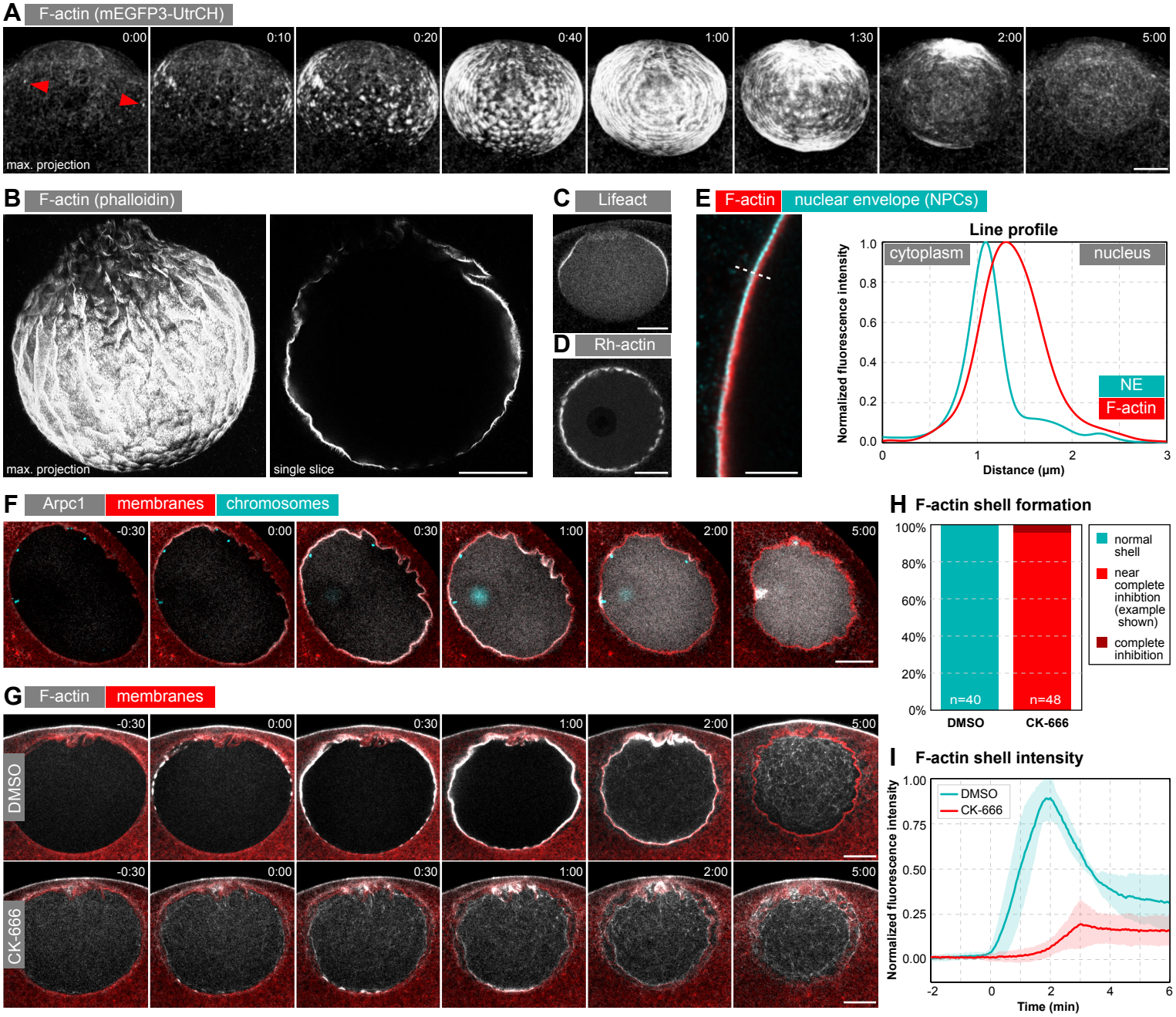
A
F-actin (mEGFP3-UtrCH)
0:00
0:10
0:20
0:40
1:00
1:30
2:00
5:00
max. projection
B
F-actin (phalloidin)
max. projection
single slice
C
Lifeact
D
Rh-actin
E
F-actin
nuclear envelope (NPCs)
Line profile
cytoplasm
nucleus
NE
F-actin
Normalized fluorescence intensity
Distance (µm)
F
Arpc1
membranes
chromosomes
-0:30
0:00
0:30
1:00
2:00
5:00
G
F-actin
membranes
DMSO
CK-666
H
F-actin shell formation
normal shell
near complete inhibtion (example shown)
complete inhibition
n=40
n=48
DMSO
CK-666
I
F-actin shell intensity
DMSO
CK-666
Normalized fluorescence intensity
Time (min)

Figure 2

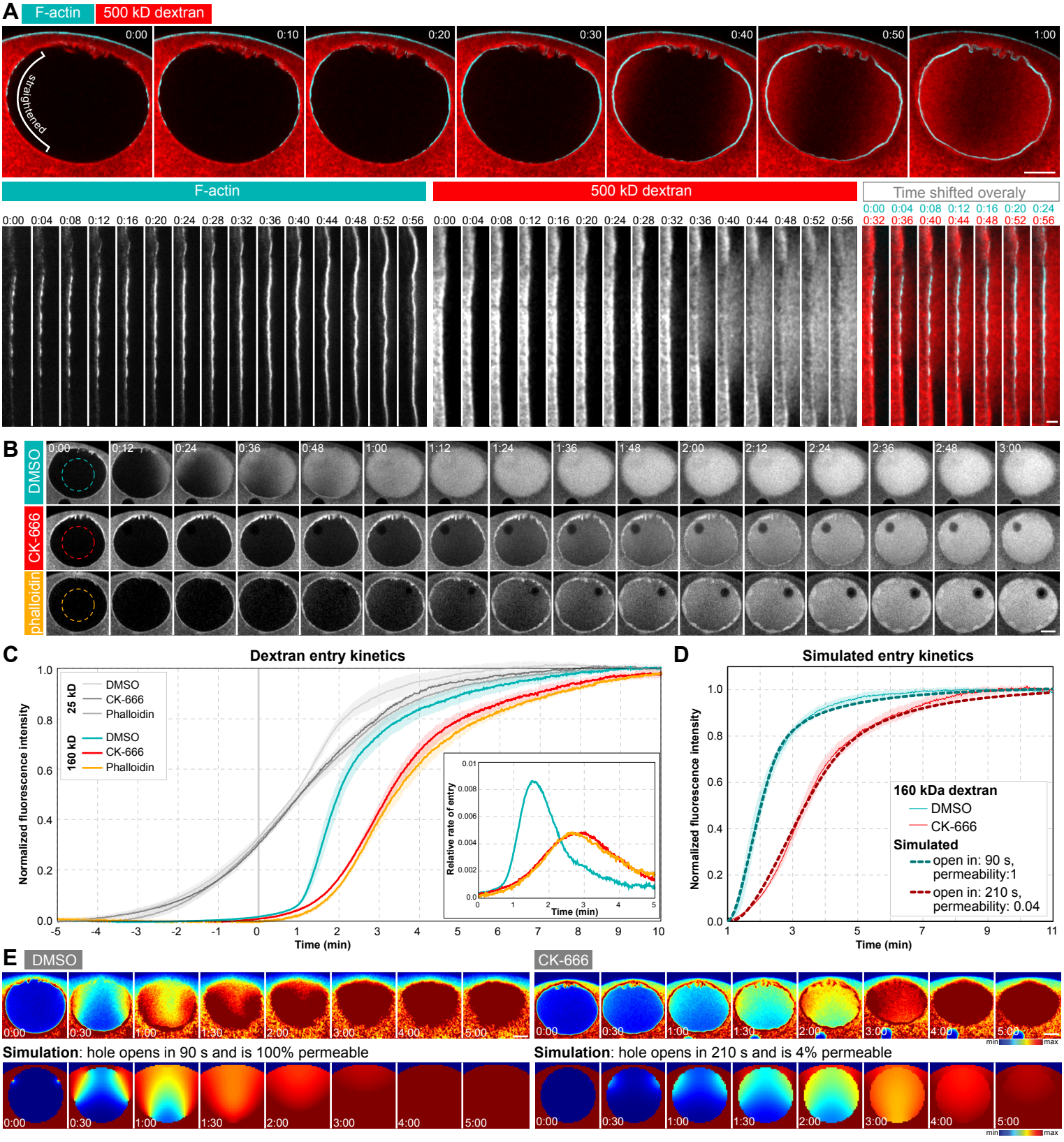
A
F-actin
500 kD dextran
0:00
0:10
0:20
0:30
0:40
0:50
1:00
straightened
F-actin
500 kD dextran
Time shifted overaly
0:00 0:04 0:08 0:12 0:16 0:20 0:24 0:28 0:32 0:36 0:40 0:44 0:48 0:52 0:56
B
DMSO
CK-666
phalloidin
0:00
0:12
0:24
0:36
0:48
1:00
1:12
1:24
1:36
1:48
2:00
2:12
2:24
2:36
2:48
3:00
C
Dextran entry kinetics
Normalized fluorescence intensity
Time (min)
25 kD
DMSO
CK-666
Phalloidin
160 kD
DMSO
CK-666
Phalloidin
Relative rate of entry
Time (min)
D
Simulated entry kinetics
Normalized fluorescence intensity
Time (min)
160 kDa dextran
DMSO
CK-666
Simulated
open in: 90 s, permeability:1
open in: 210 s, permeability: 0.04
E
DMSO
CK-666
0:00
0:30
1:00
1:30
2:00
3:00
4:00
5:00
min
max
Simulation: hole opens in 90 s and is 100% permeable
Simulation: hole opens in 210 s and is 4% permeable

Figure 3

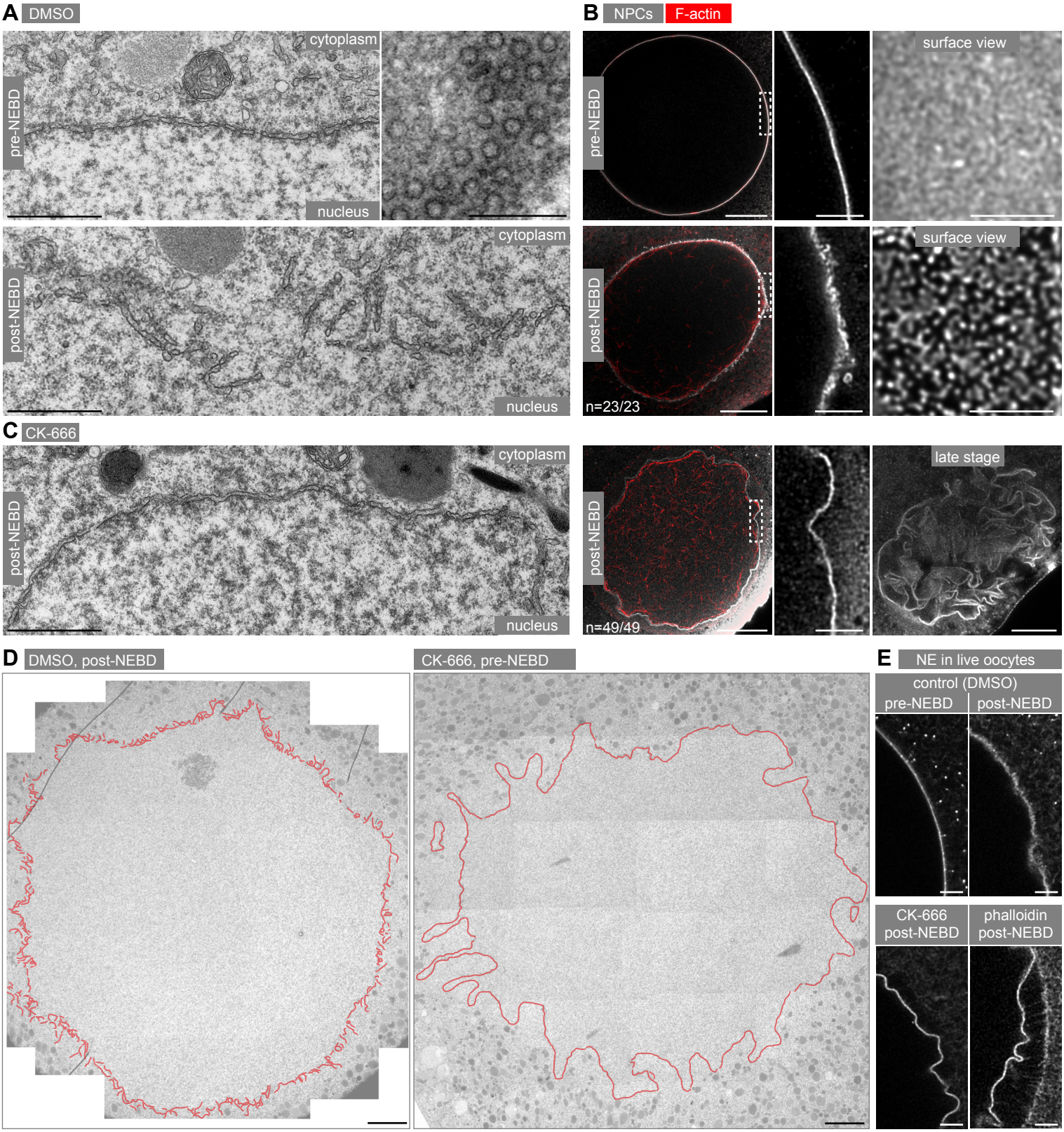
A
DMSO
cytoplasm
pre-NEBD
nucleus
cytoplasm
post-NEBD
nucleus
B
NPCs
F-actin
pre-NEBD
surface view
post-NEBD
surface view
n=23/23
C
CK-666
cytoplasm
post-NEBD
nucleus
post-NEBD
late stage
n=49/49
D
DMSO, post-NEBD
CK-666, pre-NEBD
E
NE in live oocytes
control (DMSO)
pre-NEBD
post-NEBD
CK-666
post-NEBD
phalloidin
post-NEBD

Figure 4

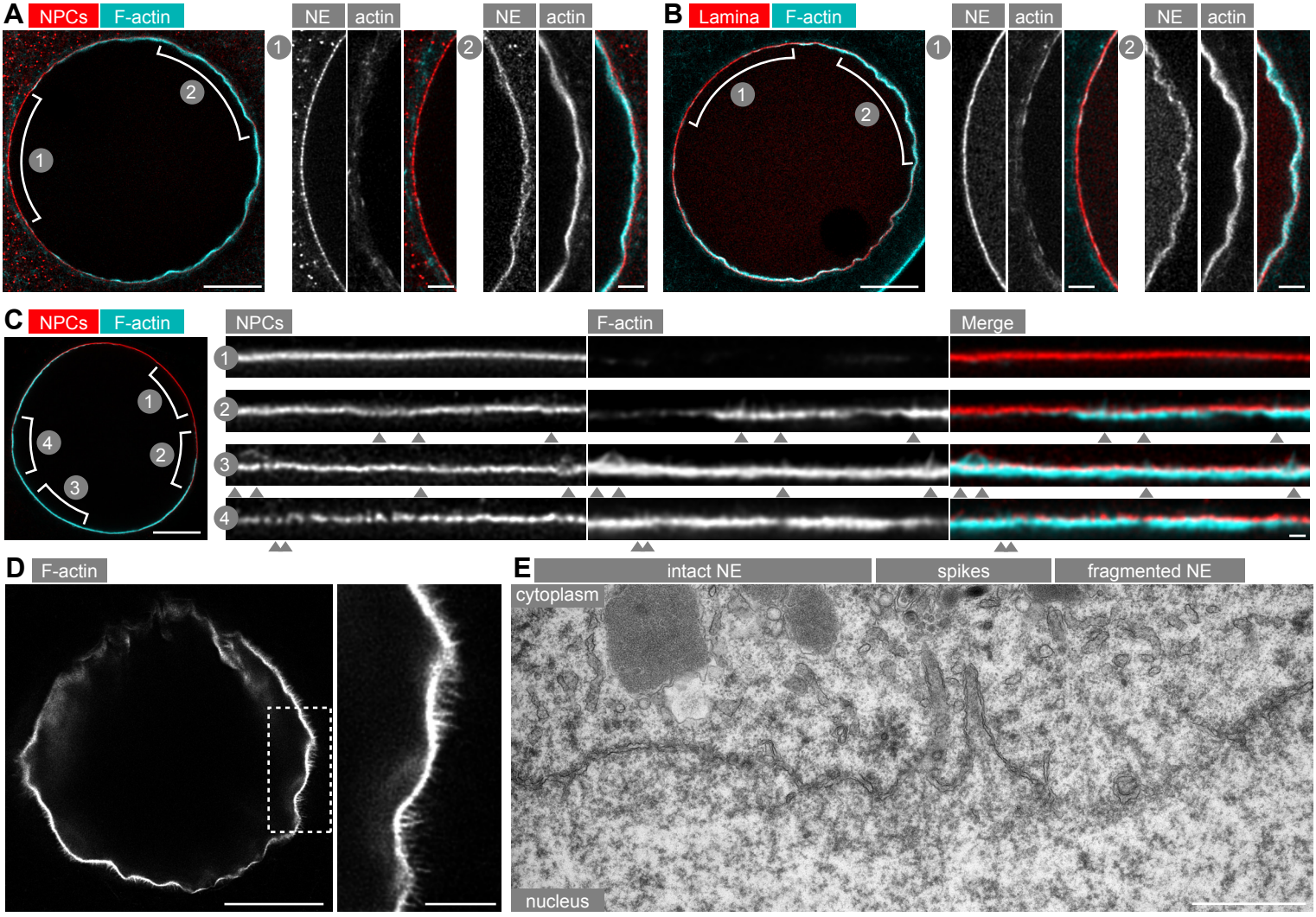
A
NPCs
F-actin
NE
actin
NE
actin
B
Lamina
F-actin
NE
actin
NE
actin
C
NPCs
F-actin
NPCs
F-actin
Merge
D
F-actin
E
intact NE
spikes
fragmented NE
cytoplasm
nucleus

Supplemental Data

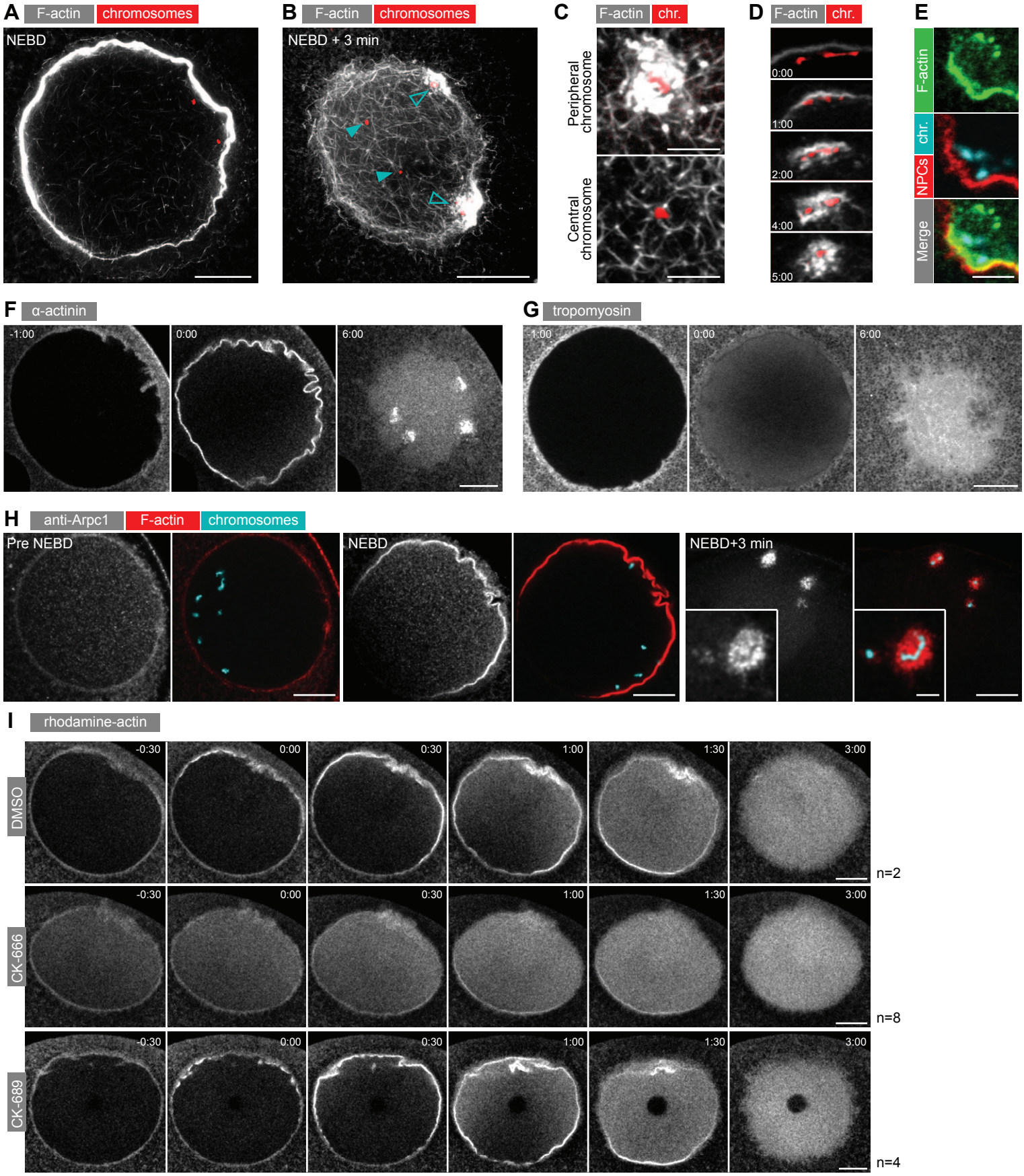

Supplementary Figure S1 (related to Figure 1). The F-actin shell and network form concomitantly, but are distinct in structure and molecular composition; the F-actin shell is stabilized on peripheral chromosomes forming dense patches of F-actin

(A) *The F-actin bundle network begins to form in the nuclear region concomitantly with the F-actin shell.* An oocyte fixed and imaged as in Figure 1B, but with the brightness enhanced to reveal the much dimmer F-actin bundles in the nuclear region. The oocyte is co-stained with phalloidin to label F-actin (gray) and DRAQ5 to label DNA/chromosomes (red). A confocal section from a 3D stack is shown; scale bar is 20 μm.

(B) *Dense patches of F-actin form on peripheral chromosomes.* An oocyte fixed 3 min after NEBD, after disassembly of the F-actin shell, and stained and imaged as in (A). Open cyan arrowheads mark F-actin patches around peripheral chromosomes; filled arrowheads mark central chromosomes without an F-actin patch.

(C) Enlarged view of a peripheral versus a central chromosome from a dataset as in (B), showing the dense patch of F-actin that is specific to peripheral chromosomes. Scale bars are 5 μm.

(D) *The F-actin shell is converted into the chromosomal patches.* Selected region of the NE adjacent to a peripheral chromosome from a live cell recording of an oocyte expressing 3mEGFP-UtrCH to label F-actin and injected with H1-Alexa647 to label chromosomes, showing the transformation of the transient F-actin shell into the denser chromosomal patch. Time is mm:ss relative to NEBD.

(E) *Peripheral chromosomal patches are in direct contact with the NE.* Selected region of the NE adjacent to a peripheral chromosome in an oocyte fixed 3 min after NEBD and stained with mAb414 to label NPCs (red), phalloidin to label F-actin (green), and DRAQ5 to label chromosomes (cyan). Scale bar is 5 μm.

(F, G) *The F-actin shell and chromosome patches have distinct molecular composition from the bundle network.* Confocal sections through the nuclear region of live oocytes expressing α-actinin-mEGFP (F) or injected with tropomyosin-Alexa568 (G). α-actinin, a filament cross-linker typically associated with Arp2/3 nucleated networks, localizes to the shell and patches but not to the bundle network; tropomyosin, which preferentially binds to long formin-nucleated F-actin bundles, localizes to the bundle network in the nuclear region but not to the shell and chromosome patches. Time is given as mm:ss relative to NEBD; scale bars are 20 μm.

(H) *Endogenous Arp2/3 complex localizes to the F-actin shell and chromosome patches.* Immuno-fluorescence staining of Arpc1 (gray), phalloidin to label F-actin (red), and DRAQ5 to label chromosomes (cyan) in oocytes fixed either before NEBD, at NEBD, or 3 minutes after NEBD. The Arpc1 staining pattern seen before NEBD represents the background staining that is always visible with this antibody independent of the stage at which the oocyte is fixed prior to NEBD. Scale bars are 20 μm, 5 μm for the inset.

(I) *Inhibition of the F-actin shell is specific to CK-666, not its inactive analog CK-689, and is observed by directly labeling actin monomers.* Confocal sections through the nuclear regions of live oocytes injected with rhodamine-actin (gray) and incubated for 1 h with 1 mM CK-666, 1 mM CK-689 or a corresponding amount of DMSO prior to NEBD. Times are given as mm:ss relative to NEBD; scale bars are 20 μm. The number of oocytes tested under each condition is indicated at the far right.

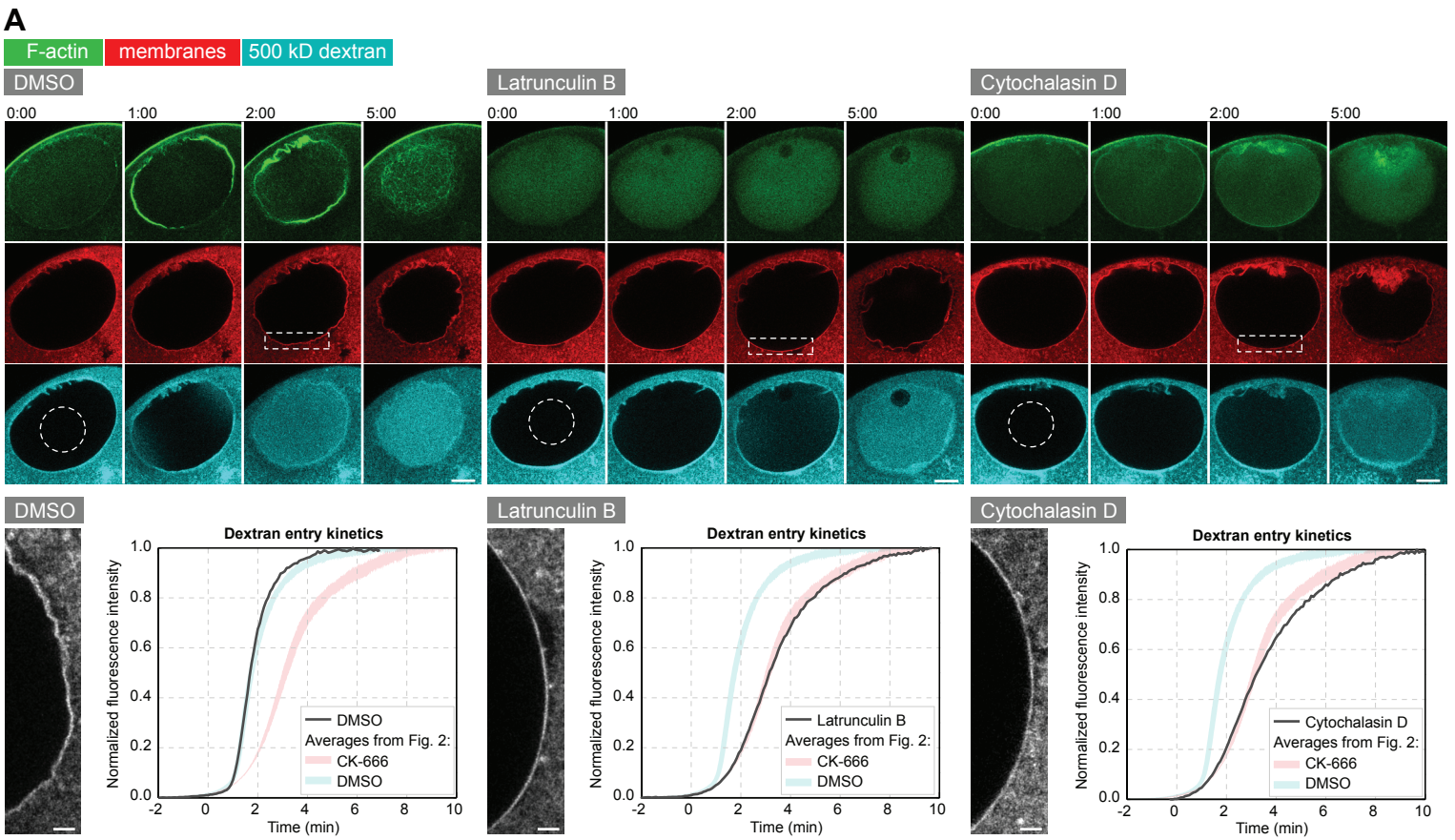
A
F-actin
membranes
500 kD dextran
DMSO
Latrunculin B
Cytochalasin D
0:00
1:00
2:00
5:00
Dextran entry kinetics
Normalized fluorescence intensity
Time (min)
DMSO
Averages from Fig. 2:
CK-666
DMSO
Latrunculin B
Cytochalasin D

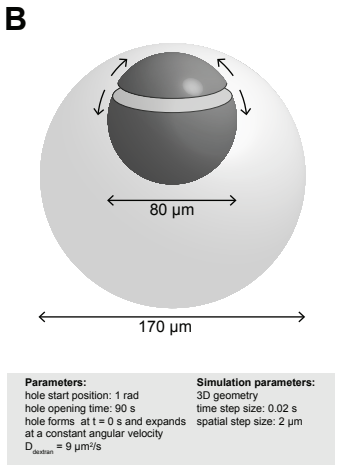
B
80 µm
170 µm
Parameters:
hole start position: 1 rad
hole opening time: 90 s
hole forms at t = 0 s and expands at a constant angular velocity
D dextran = 9 µm²/s
Simulation parameters:
3D geometry
time step size: 0.02 s
spatial step size: 2 µm

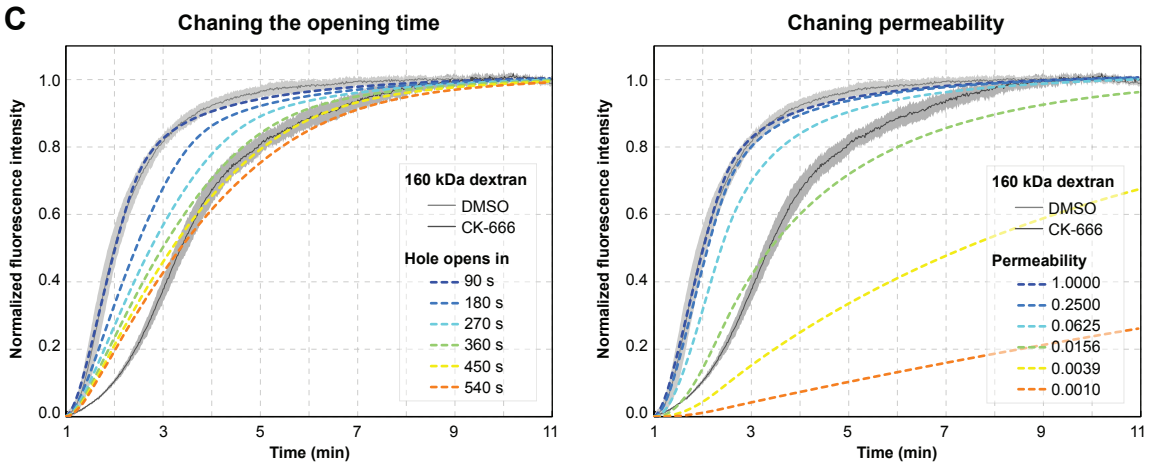
C
Chaning the opening time
Chaning permeability
Normalized fluorescence intensity
Time (min)
160 kDa dextran
DMSO
CK-666
Hole opens in
90 s
180 s
270 s
360 s
450 s
540 s
Permeability
1.0000
0.2500
0.0625
0.0156
0.0039
0.0010

Supplementary Figure S2 (related to Figure 2). Inhibition of the F-actin shell delays entry of large cytoplasmic molecules

(A) *Depolymerization of F-actin by cytochalasin D or latrunculin B delays dextran entry and blocks NE fragmentation in a manner indistinguishable from Arp2/3 inhibition by CK-666*. *Upper panels:* Confocal sections through the nuclear region of live oocytes expressing 3mEGFP-UtrCH (green) and injected with $DiIC_{18(3)}$ (red) to label endomembranes and Cy5-500 kD dextran (cyan) to monitor NE permeability. Oocytes were treated with either latrunculin B (10 µM, 10 min before NEBD), cytochalasin D (10 µM, 3 min before NEBD), or an equal amount of DMSO as a control. Time is given as mm:ss relative to NEBD, scale bars are 20 µm. *Lower panels:* Enlarged regions of the NE (marked with dashed rectangles above) from the $DiIC_{18(3)}$ channel at 2 minutes post-NEBD; scale bars are 5 µm. Plots of dextran entry kinetics (as described in Figure 2C) measured within the dashed circles above are shown for the 500 kD dextran (solid black lines), compared to the kinetics observed for CK-666 treatment and DMSO controls in Figure 2C (pink and blue regions).

(B) *Illustration of the geometry and key parameters of the dextran entry simulation.* The oocyte is modeled as a 170 µm diameter sphere containing a 80 µm spherical nucleus located 5 µm from the surface of the larger sphere at the point of closest approach (corresponding to the animal pole). At NEBD, a ring shaped region of permeablization is created in the spherical nucleus; the ring is initially positioned perpendicular to the animal-vegetal axis at 1 rad angle and a specified permeability to dextran (set to 1 in control oocytes). The ring then expands with a constant angular velocity until it encompasses the entire nucleus in a total time defined as the "opening time" (90 s in control oocytes). We set the values of these parameters based on our measurements of dextran entry in high resolution 3D imaging datasets. We then fit the diffusion coefficient of the dextran in the simulation to match the observed dextran entry kinetics in control oocytes. The fit value of 9 $\mu m^2/s$ matches the value expected from earlier fluorescence correlation spectroscopy (FCS) measurements of 160 kD dextran diffusion [S1].

(C) *Effect of varying the opening time and permeability parameters.* Simulated dextran entry kinetics (dashed colored lines) compared to the normal (solid gray line) and delayed entry kinetics observed upon inhibition of the F-actin shell by treatment with CK-666 (solid black line), showing that the delayed entry kinetics cannot be explained by changing a single parameter. The result of fitting the delayed entry kinetics by varying both parameters is shown in Figure 2D.

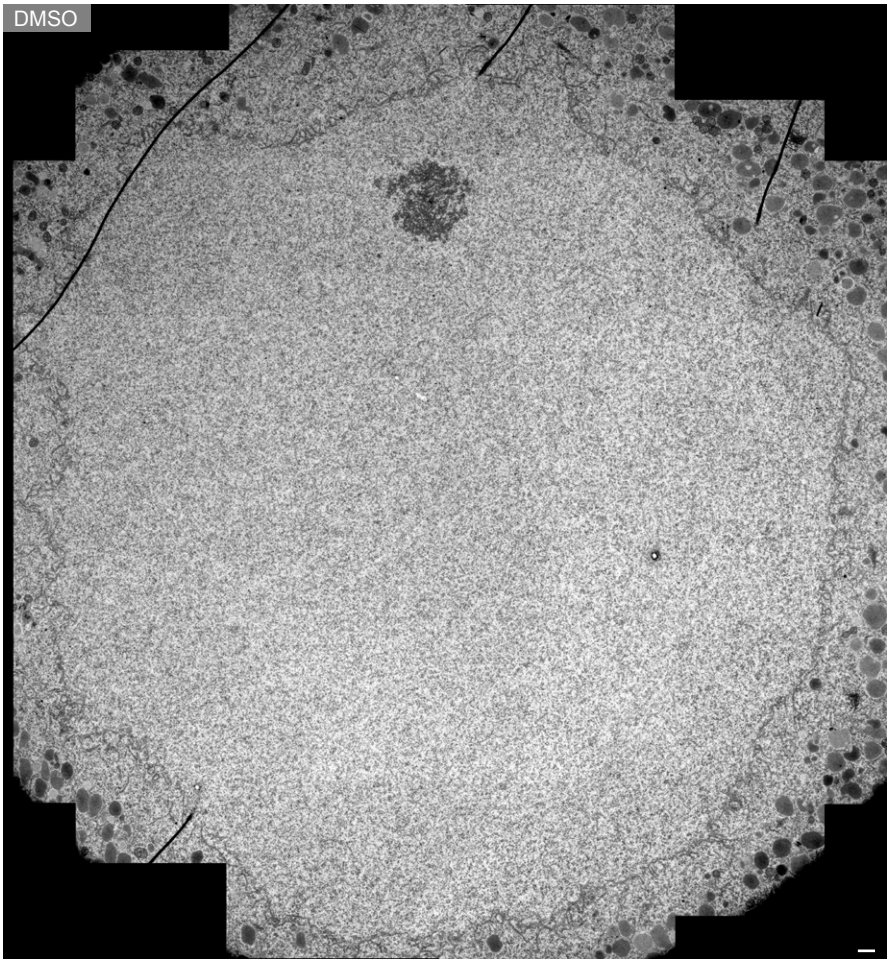
DMSO

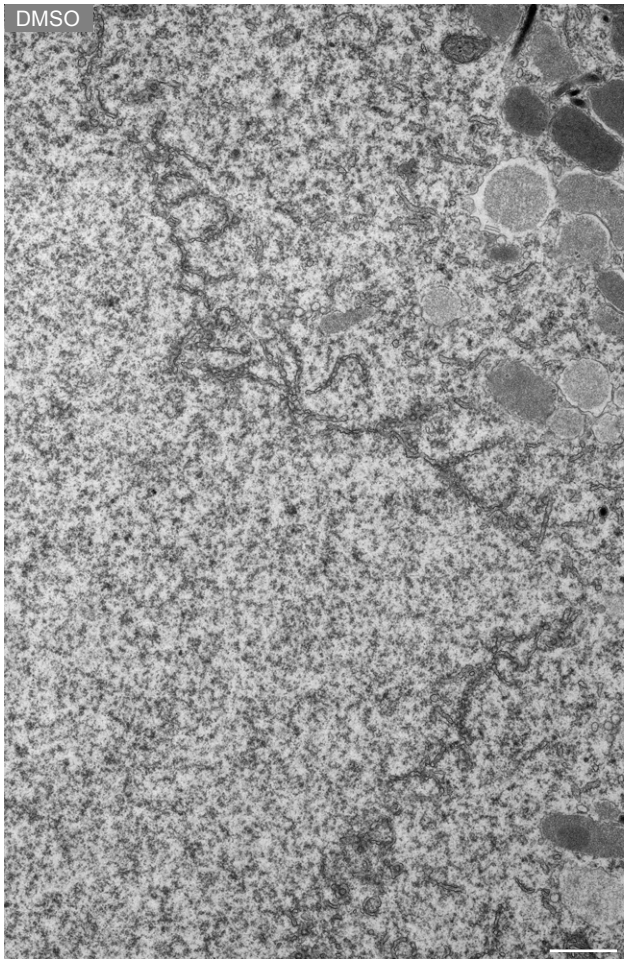
DMSO

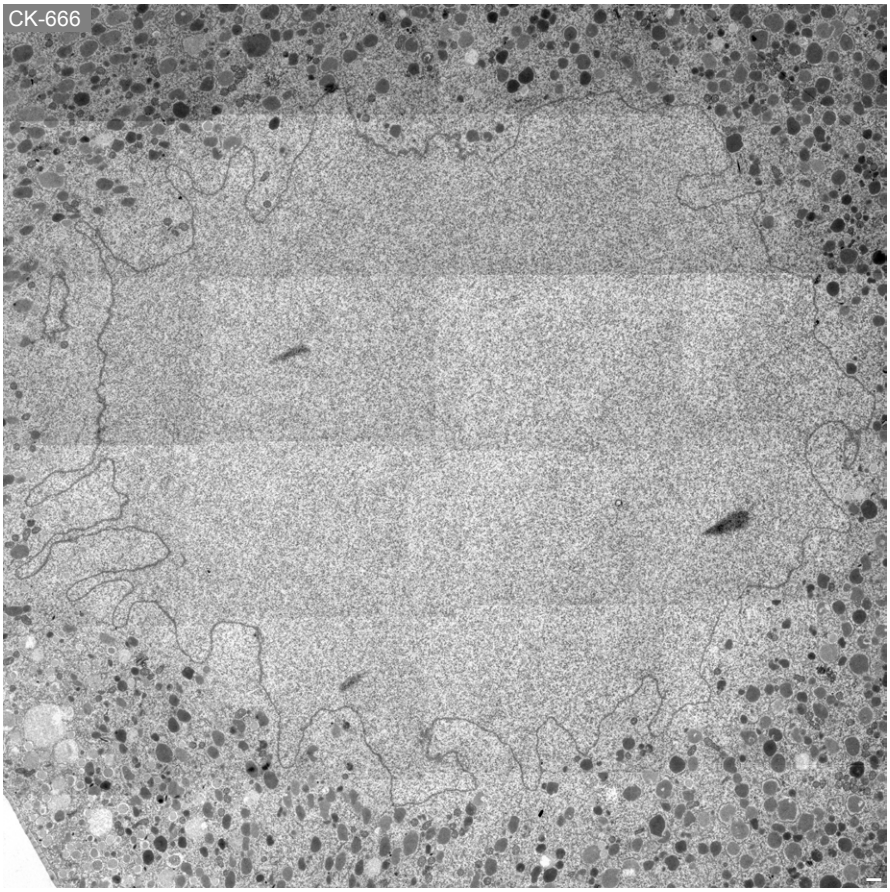
CK-666

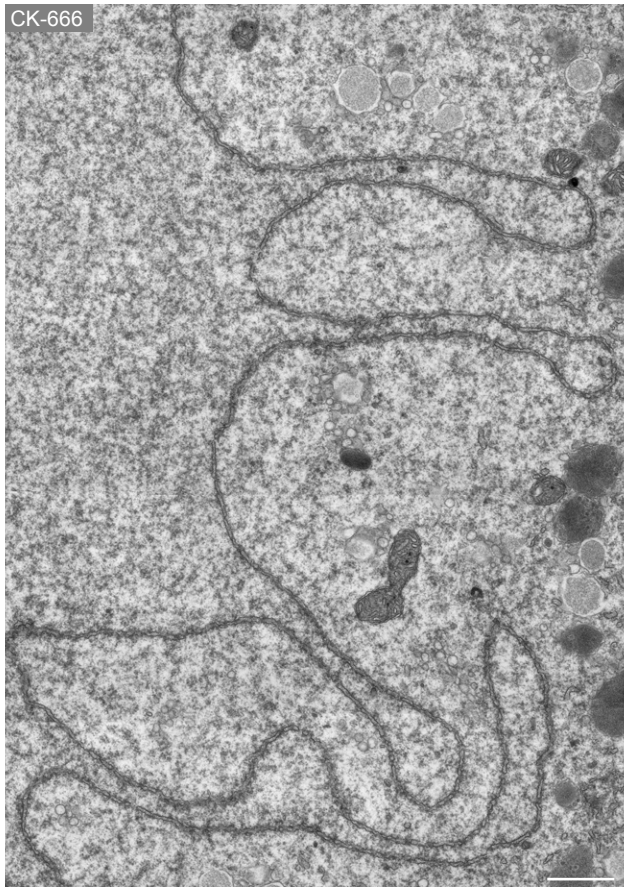
CK-666

Supplementary Figure S3 (related to Figure 3). Electron micrograph montages

Thin section EM montages of the entire nuclear region of oocytes fixed after NEBD and treated with CK-666 (bottom) or a corresponding concentration of DMSO as a control (top). Enlarged regions of the NE are shown on the right. The NE fragments in these montages are traced in Figure 3D.

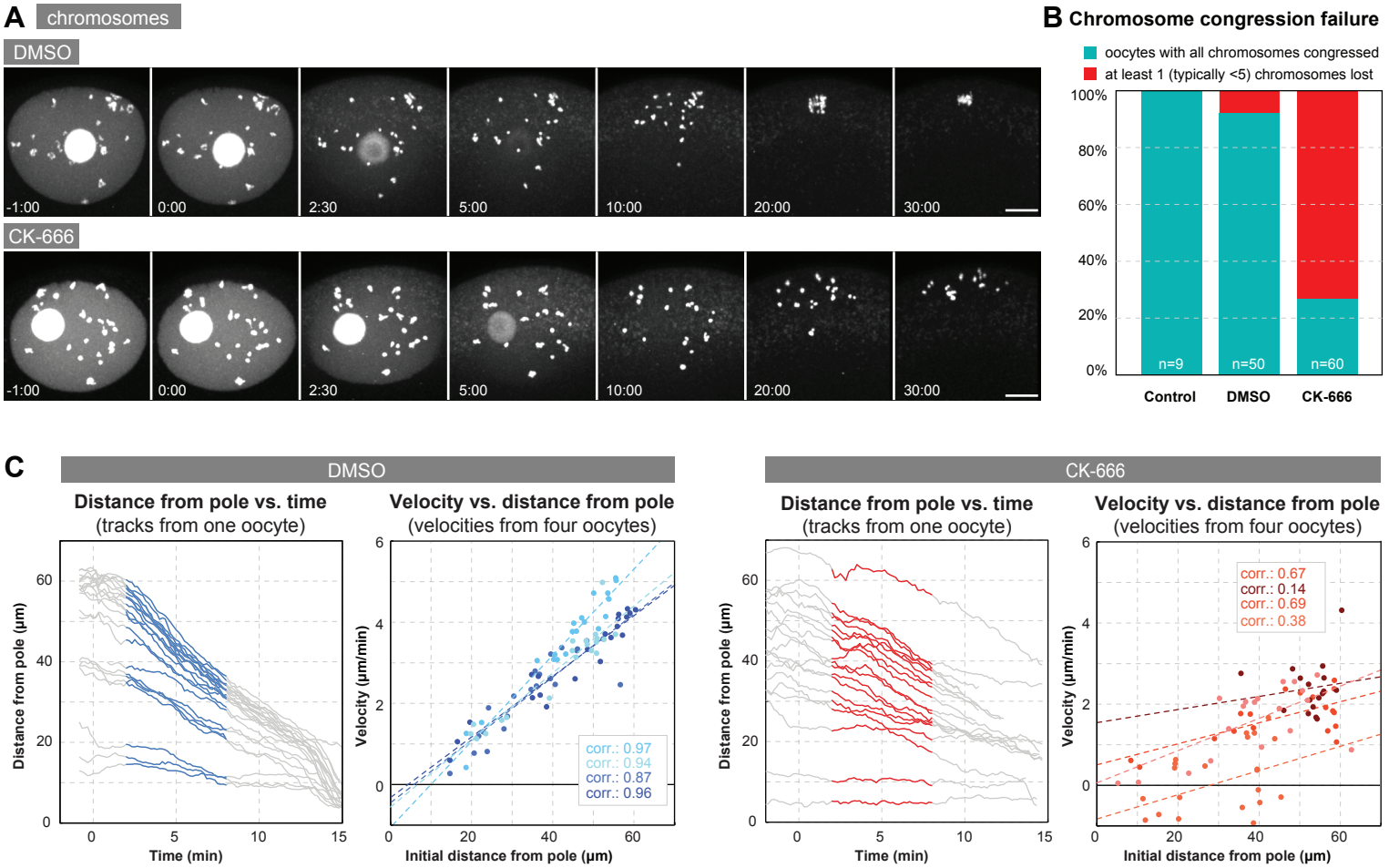
A
chromosomes
DMSO
-1:00
0:00
2:30
5:00
10:00
20:00
30:00
CK-666
-1:00
0:00
2:30
5:00
10:00
20:00
30:00
B Chromosome congression failure
oocytes with all chromosomes congressed
at least 1 (typically <5) chromosomes lost
100%
80%
60%
40%
20%
0%
n=9
n=50
n=60
Control
DMSO
CK-666
C
DMSO
Distance from pole vs. time
(tracks from one oocyte)
Distance from pole (µm)
Time (min)
Velocity vs. distance from pole
(velocities from four oocytes)
Velocity (µm/min)
Initial distance from pole (µm)
corr.: 0.97
corr.: 0.94
corr.: 0.87
corr.: 0.96
CK-666
Distance from pole vs. time
(tracks from one oocyte)
Distance from pole (µm)
Time (min)
Velocity vs. distance from pole
(velocities from four oocytes)
Velocity (µm/min)
Initial distance from pole (µm)
corr.: 0.67
corr.: 0.14
corr.: 0.69
corr.: 0.38

Supplementary Figure S4 (related to Figure 4). Blocking NE fragmentation leads to aneuploidy

(A) Maximum intensity Z-projections through the nuclear region of live oocytes expressing H2B-EGFP to label chromosomes and treated with either CK-666 or DMSO as a control. Time is given as mm:ss relative to NEBD; scale bars: 20 µm.

(B) Percent of oocytes with at least one lost chromosome under the following conditions: untreated (control), incubated with DMSO, or incubated with CK-666. Oocytes were imaged through meiosis (as in (A)) until polar body formation, and chromosomes not captured and aligned on the metaphase plate were counted as 'lost' (defined as a distance of at least 10 µm from the metaphase plate). n is the number of oocytes analyzed for each treatment condition.

(C) Chromosome positions from 3D imaging of oocytes expressing H2B-mCherry (as in (A)) were tracked as previously described [S2]. The distance of each chromosome from the animal pole is plotted over time for both DMSO treated control and CK-666 treated oocytes (left panel for each condition). Each distance plot includes tracks from a single oocyte. The average velocity of each chromosome (measured from 2-8 min after NEBD; colored portions of the lines) is plotted versus its initial distance from the animal pole (right), with velocities from 4 oocytes superimposed for each condition. As shown previously, normal (undisrupted) contraction of the F-actin bundle network results in a reproducible linear relationship between the velocities of individual chromosomes and their initial distance from the animal pole at NEBD [S2]. This linear relationship is clearly present in control oocytes (dashed lines) but is disrupted in CK-666 treated oocytes. In addition, the chromosome velocity magnitudes are reduced roughly 2-fold in CK-666 treated oocytes as compared to control.

Supplementary Experimental Procedures

Oocyte injection, maturation and drug treatments

Starfish (*Patiria miniata*, a.k.a. *Asterina miniata*) were obtained from Southern California See Urchin Co. (Corona del Mar, CA), Marinus Scientific LLC (Newport Beach, CA) or Monterey Abalone Company (Monterey, CA) and maintained in sea water tanks at 16 °C at EMBL's Marine Facility. Oocytes were isolated and injected using mercury filled needles as previously described in [S1] (see also http://mterasaki.us/panda/injection/). Protein markers were injected shortly before initiation of meiosis, whereas mRNAs encoding fluorescent markers were injected the day before and incubated overnight at 14 °C to obtain sufficient levels of protein expression. Meiotic maturation was triggered by addition of 10 µM 1-methyladenine (Acros Organics). NEBD typically started 20 min after hormone addition, and only oocytes starting NEBD between 15 and 35 min were analyzed. For CK-666 (Calbiochem) treatments, oocytes were treated at 0.5 mM final concentration and incubated for 1 h prior to hormone addition. For the inactive control experiment, CK-666 and CK-689 were purchased from MerckMillipore and used at 1 mM final concentration the same way as above. For phalloidin injection, oocytes were injected with 3 milli-unit Alexa488-phalloidin (dissolved in water, Invitrogen) into the cytoplasm and incubated for 60 min before hormone addition. Latrunculin B (Sigma) was added at 10 µM final concentration 10 min before NEBD and cytochalasin D (Santa Cruz Biotechnology) at 10 µM final concentration 3 min before NEBD.

Live cell fluorescent markers

PolyA-tailed RNA from starfish matured eggs was reverse transcribed with GeneRacer kit (Invitrogen), and full-length cDNA for α-actinin and Arpc1 was isolated using degenerate or specific primers. α-actinin-mEGFP and mEGFP-Arpc1 were subcloned into pGEMHE for *in vitro* transcription as described earlier [S1]. Capped mRNAs were synthesized from linearized templates (using either Ambion or Cellscript kits) and extended with poly(A) tails at the 3' termini using the Poly(A) Tailing Kit (Ambion or Cellscript). mRNAs were dissolved in 11 µl RNase-free water (typically at 1-2 µg/µl) and injected to 1-5% of the oocyte volume. H2B-EGFP, H2B-mCherry, POM121-EGFP3, lamin B-GFP and mEGFP3-UtrCH constructs were described earlier [S1, S2]. Histone H1 from calf thymus (Merck) was labeled with Alexa568 or 647 succinimidyl ester (Invitrogen) as described in [S2] and was injected to 0.1% of the oocyte volume. Alexa568 labeled tropomyosin (purified from rabbit skeletal muscle, 2.29 mg/ml) was a gift from Beata Bugyi (University of Pécs, Hungary), and was injected at 3% of the oocyte volume. $DiIC_{18(3)}$ (Invitrogen) was dissolved in vegetable oil to saturation and injected to 0.1% of the oocyte volume. TRITC labeled 160 kD dextran (Sigma Aldrich) and Cy5 labeled 25 kD and 500 kD dextrans (Invitrogen) were injected to 1% of the oocyte volume. These dextrans were previously calibrated by fluorescence correlation spectroscopy (FCS) and gel filteration. Both of the larger dextrans (160 kD and 500 kD) have been shown to be markers for NE fragmentation [S1], and here they have been used interchangeably depending on which fluorescent color was best suited for a given experiment.

Immunofluorescence

For immunofluorescence, oocytes were fixed in low glutaraldehyde fixation buffer (100 mM HEPES, 50 mM EGTA, 10 mM $MgSO_4$, 0.5% Triton, 0.1% glutaraldehyde (Electron Microscopy Sciences), 1% formaldehyde (Electron Microscopy Sciences) at pH 7.0) for 1 h at room temperature. For fluorescence staining with small-molecule dyes and optimized to preserve F-actin, oocytes were fixed in high glutaraldehyde fixation buffer (100 mM HEPES, 50 mM EGTA, 10 mM $MgSO_4$, 0.5% Triton, 2% glutaraldehyde, 1% formaldehyde pH 7.0) for 1 h at room temperature. The fixed oocytes were incubated with a combination of Alexa Fluor 488 or 568 phalloidin (1:40, to label F-actin, Life technologies), DRAQ5 (1:2000, Biostatus, to label DNA), mAb414 (Covance) (1:1000, to label NPCs) or

anti-Arpc1 antiserum (1:50) for 1-2 h at room temperature or overnight at 4 °C. To obtain the Arpc1 antibody, the C-terminal domain of the starfish Arpc1 protein (212-372 a.a.) was expressed in *E. coli* (BL21, DE3) as a C-terminal His6 fusion protein (pET24d, Novagen) and purified with Ni-NTA Resin (Qiagen). Anti-starfish Arpc1 rabbit polyclonal antibody was then raised against this recombinant protein, and was affinity-purified with the antigen.

Electron microscopy

Oocytes were fixed in 1% glutaraldehyde in sea water for 2 h, rinsed in sea water, and stored at 4 °C. Oocytes were subsequently postfixed with 1% OsO_4 and 0.8% potassium ferricyanide in cacodylate buffer, rinsed thoroughly in distilled water, and stained in 0.5% aqueous uranyl acetate for 1 h. They were dehydrated in acetone and embedded in EPON (Serva). 70 nm sections were stained with uranyl acetate and lead citrate and examined in a transmission electron microscope (BioTwin; Philips).

Light microscopy and image processing

Microscopy was done either on a customized SP5 (Leica) or LSM780 (Zeiss) confocal microscope equipped with a fast Z-focusing device (SuperZ Galvo stage or objective piezo) and using 40x HCX PL APO 1.10 NA, 63x HC PL APO 1.30 NA (Leica) or 40x C-Apochromat 1.2 NA (Zeiss) water or glycerol immersion objective lenses.

Figures show selected images from time and/or z-series following brightness and contrast adjustment and application of a Gaussian blur filter (0.5-1 pixels) to reduce shot noise. To ease visualization of curved NE outlines, in some cases (as noted in the text) these were straightened using the "straighten" function of ImageJ (http://rsbweb.nih.gov/ij/). Wherever mentioned, images were deconvolved using a theoretical point-spread-function in the Huygens Software (Scientific Volume Imaging B.V.). For measuring mean intensities, raw images were analyzed in ImageJ either using manually defined ROIs or ROIs automatically segmented on the $DiIC_{18(3)}$ channel using the level sets algorithm (http://fiji.sc/Level_Sets). Chromosome tracking was done as described earlier in [S2]. Unless stated otherwise, all images were processed in ImageJ and subsequently assembled in Adobe Illustrator (Adobe). Data analysis was done using Matlab (Mathworks) and Excel (Microsoft).

Computer simulation of diffusion with barriers

The diffusion of dextran within a compartmentalized volume was calculated over a 3D regular square grid using finite differences and a simple Euler forward integration scheme. Three regions were defined: outside, cytoplasmic and nuclear. Each cubic volume element was attributed to one of these regions, depending on the position of the center of the volume. Scalar quantity u_i^t represented the concentration of dextran contained within the volume ***i*** at time ***t***. The evolution of these quantities was calculated according to the laws of diffusion:

$$u_i^{t+\tau} = u_i^t + \frac{D\tau}{\delta^2}\sum_j c_{ij}(u_j^t - u_i^t)$$

The sum is over all elements ***j*** sharing a face with ***i***, where the coefficients $c_{ij} \in [0,1]$ are used to represent the fraction of the barrier that is open between ***i*** and ***j***. If $c_{ij} = 0$, dextran may not be exchanged between the two cells, while if $c_{ij} = 1$, diffusion is unconstrained. The coefficients c_{ij} are set to 1 for two volume elements ***i*** and ***j*** both belonging to the cytoplasm or to the nucleus, and to zero if one of the volumes is outside the oocyte. The coefficients between cytoplasmic and nuclear volume elements are set to ***p*** (the permeability) if the border between the elements is within the 'open region' of the NE, and 0 otherwise. The 'open region' is a ring on the spherical NE defined by two angles that change with a constant rate, until the open region expands to cover the entire NE.

The simulation was implemented in C++ within *cytosim* (www.cytosim.org) with a grid size and time step sufficiently small to ensure valid results, and the calculation time was a few minutes on a laptop. The source code is available upon request from the authors.

Supplementary references

S1. Lénárt, P., Rabut, G., Daigle, N., Hand, A. R., Terasaki, M., and Ellenberg, J. (2003). Nuclear envelope breakdown in starfish oocytes proceeds by partial NPC disassembly followed by a rapidly spreading fenestration of nuclear membranes. J. Cell Biol. *160*, 1055–1068.

S2. Mori, M., Monnier, N., Daigle, N., Bathe, M., Ellenberg, J., and Lénárt, P. (2011). Intracellular transport by an anchored homogeneously contracting f-actin meshwork. Curr. Biol. CB *21*, 606–611.